OPEN ACCESS
IOP Publishing
Measurement Science and Technology
Meas. Sci. Technol. **27** (2016) 104001 (17pp)
doi:10.1088/0957-0233/27/10/104001

Development and application of optical fibre strain and pressure sensors for in-flight measurements

N J Lawson[1], R Correia[2], S W James[2], M Partridge[2], S E Staines[2], J E Gautrey[1], K P Garry[3], J C Holt[3] and R P Tatam[2]

[1] National Flying Laboratory Centre, Cranfield University, Cranfield, Bedford MK43 0AL, UK
[2] Engineering Photonics, Cranfield University, Cranfield, Bedford MK43 0AL, UK
[3] Centre for Aeronautics, Cranfield University, Cranfield, Bedford MK43 0AL, UK

E-mail: n.lawson@cranfield.ac.uk

Received 31 May 2015, revised 18 April 2016
Accepted for publication 13 June 2016
Published 16 September 2016

Abstract

Fibre optic based sensors are becoming increasingly viable as replacements for traditional flight test sensors. Here we present laboratory, wind tunnel and flight test results of fibre Bragg gratings (FBG) used to measure surface strain and an extrinsic fibre Fabry–Perot interferometric (EFFPI) sensor used to measure unsteady pressure. The calibrated full scale resolution and bandwidth of the FBG and EFFPI sensors were shown to be 0.29% at 2.5 kHz up to 600 $\mu\varepsilon$ and 0.15% at up to 10 kHz respectively up to 400 Pa. The wind tunnel tests, completed on a 30% scale model, allowed the EFFPI sensor to be developed before incorporation with the FBG system into a Bulldog aerobatic light aircraft. The aircraft was modified and certified based on Certification Standards 23 (CS-23) and flight tested with steady and dynamic manoeuvres. Aerobatic dynamic manoeuvres were performed in flight including a spin over a g-range $-1g$ to $+4g$ and demonstrated both the FBG and the EFFPI instruments to have sufficient resolution to analyse the wing strain and fuselage unsteady pressure characteristics. The steady manoeuvres from the EFFPI sensor matched the wind tunnel data to within experimental error while comparisons of the flight test and wind tunnel EFFPI results with a Kulite pressure sensor showed significant discrepancies between the two sets of data, greater than experimental error. This issue is discussed further in the paper.

Keywords: flight test, fibre Bragg grating, extrinsic fibre Fabry–Perot interferometer

(Some figures may appear in colour only in the online journal)

Nomenclature

FBG	Fibre Bragg grating
EFFPI	Extrinsic fibre Fabry–Perot interferometer
V	Aircraft velocity
AHRS	Attitude heading reference system
$(n-1)$	Normal g increment
C_{FP}	EFFPI calibration coefficient (nm Pa^{-1})
C_p	Pressure coefficient
p	Sensor pressure (Pa)
T	Sensor temperature (K)

Original content from this work may be used under the terms of the Creative Commons Attribution 3.0 licence. Any further distribution of this work must maintain attribution to the author(s) and the title of the work, journal citation and DOI.

1. Introduction

The field of civil aircraft flight testing presents many instrumentation challenges, including the scale, the environment and the regulatory requirements [1, 2]. In terms of scale, with aircraft such as the Airbus A380, measurements may need to be taken from areas of the aircraft which are up to 100 m from the hardware and processor boxes. The main measurement

 © 2016 IOP Publishing Ltd Printed in the UK

variables of interest for basic aerodynamic analysis of the aircraft are geometry, strain, pressure and temperature. In this case, established flight test techniques use traditional methods such as photogrammetry for shape measurement [3], unsteady piezoresitive sensors such as Kulites for pressure measurement [4], resistive foil strain gauges for the measurement of surface strain [5] and thermocouples for surface temperature measurement [6]. The electromagnetic compatibility (EMC) requirements as specified in the certification standards such as CS-23 or CS-25 and the nature of some of these instruments can also prove challenging when fitting the instruments onto the test aircraft [2].

The potential of fibre Bragg grating (FBG) sensors for use in aerospace applications, including wind tunnel and aircraft structural health monitoring [7–11] and wing shape measurement [12, 13], is now becoming widely acknowledged. The key benefits of FBGs include their immunity to electromagnetic interference, the low weight of the sensor elements, the ability to embed optical fibres into composite materials or to surface mount to metals, the ability to multiplex an array of sensors in a single optical fibre and the ability to monitor several arrays simultaneously using an appropriately configured sensor demodulation system.

In work by Read and Foote [11], FBG sensors configured in the equivalent of a strain gauge delta rosette, with an additional sensor arranged to be sensitive to only temperature, were mounted on a backing material to form a surface mounted patch. Seven patches were mounted on the underside of the wing of a Jetstream 31 aircraft, with the sensors interrogated using an acousto-optic tuneable filter based system, capable of monitoring 27 FBGs, including one reference grating, at a data rate of 25 Hz with a strain range of $\pm 3000\ \mu\varepsilon$ and temperature range −35 °C to 85 °C. NASA reported [12, 13], a wing shape measurement system based on multiple FBGs glued to a series of wing surface points, in a spatial matrix which allowed multiple surface strain measurements to be taken on the ground and in flight. These strain measurements were subsequently used to calculate the wing shape from a wing bending model.

The measurement of pressure for aerospace applications, more specifically unsteady static pressure, using fibre optic methods has been less widely reported than has the use of FBGs for measuring strain. Where conventional pressure sensor systems generally measure the pressure-induced deformation of a flexible diaphragm by attaching strain gauges to the diaphragm, fibre optic pressure sensors are most often based on extrinsic fibre Fabry–Perot interferometers (EFFPI) [14, 15]. As the optical cavity is formed between the distal end of the optical fibre and the diaphragm, the sensor is down lead insensitive. The device can also be compact, with dimensions similar to that of the cross-section of the optical fibre (100 s of microns) [16], and can offer high bandwidths [17]. For example, EFFPI devices have been used to monitor pressure in gas turbine applications. In one case, EFFPIs were embedded in the trailing edge of nozzle guide vane upstream of a rotor in a full-scale turbine test facility, with the sensor operating over a range 0–600 kPa, with a noise floor of 0.65 kPa. This EFFPI system was shown to be capable of resolving flow structure at the blade passing frequency (8 kHz) [18]. EFFPIs have also been embedded in the wall of a compressor test rig to monitor pressure during testing of a transonic fan [19]. EFFPI sensors have been deployed to measure strain and pressure on a rotor blade in a spin chamber, using a sensor demodulation system mounted in the rotating frame with wireless data transfer [20], and have been evaluated in shock tubes [18] and wind tunnels [21], where it was found that the adhesive used to bond the diaphragm to the fibre ferrule influenced the dynamic response. At the time of writing, however, the authors believe no EFFPI systems have been applied in-flight on aircraft.

This paper describes the development and application of an FBG strain sensor and an EFFPI unsteady pressure sensor for aerospace applications. The techniques underwent laboratory and wind tunnel tests prior to flight testing on a light aircraft test bed. In-flight, the two instruments are shown to perform well under dynamic and steady state conditions through a g-load range of −1g to +4g, offering the potential for application to larger scale aircraft.

2. Development of fibre optic sensors for flight test

2.1. Fibre Bragg grating system

A fibre Bragg grating (FBG) is a periodic modulation of the refractive index of the core of an optical fibre, which acts to reflect a specific wavelength (the Bragg wavelength, which is dependent upon the period of the grating and the refractive index of the propagating mode) back along the optical fibre. The reflected Bragg wavelength is sensitive to perturbation of the grating structure by environmental parameters such as strain and temperature, and the basis of FBG sensors is the measurement of the Bragg wavelength. A major advantage of FBG technology is an array of uniquely identifiable sensors can be created within a single length of optical fibre by fabricating each FBG in the array with a different grating period, and thus different Bragg wavelength at quiescent conditions [22–24]. Using this multi-grating method, Technobis Fibre Technologies and Nederlands Lucht- en Ruimtevaartcentrum (NLR) have reported a flight test of an FBG demodulator capable of monitoring 4 arrays of sensors, with 8 sensors in each array, with a sample rate of 19.3 kHz [25, 26]. Using similar FBG techniques, the measurement of temperature would also be possible.

5 FBGs were fabricated in SMF-28 optical fibre that had been hydrogen loaded to increase its photosensitivity. The fibre was side-illuminated via a phase mask using the 266 nm output from a frequency quadrupled flashlamp pumped Nd:YAG laser. A different phase mask was used for the fabrication of each FBG, such that, in their quiescent states, the FBGs were of different Bragg wavelengths, and thus could be multiplexed in the wavelength domain. Prior to exposure, the polyacrylate buffer jacket was removed from the sections of fibre into which the FBGs were to be written. Each FBG was of length 4 mm with a typical reflectivity of 50% and 3 dB bandwidth of 0.5 nm. The FBGs were not recoated.

The laboratory calibration of the FBG sensors was completed using an Instron mechanical test bench with the sensor mounted onto a 25 mm by 200 mm aluminium test plate with

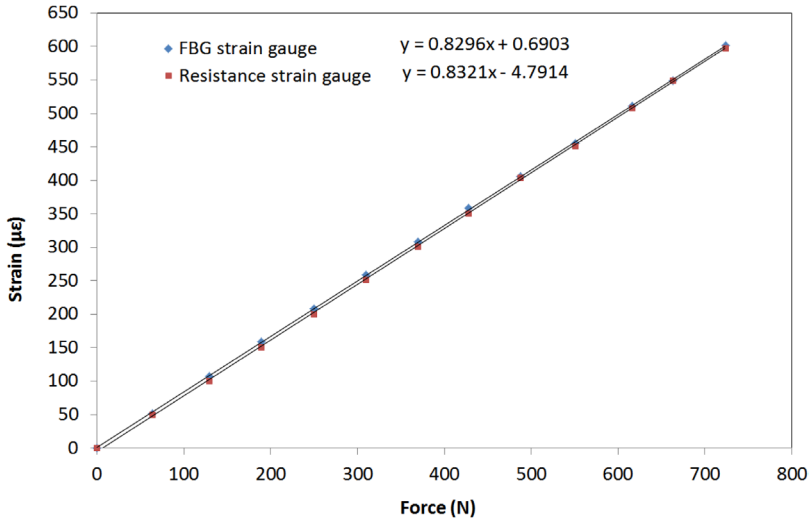

Figure 1. FBG and resistance foil strain gauge calibration curves.

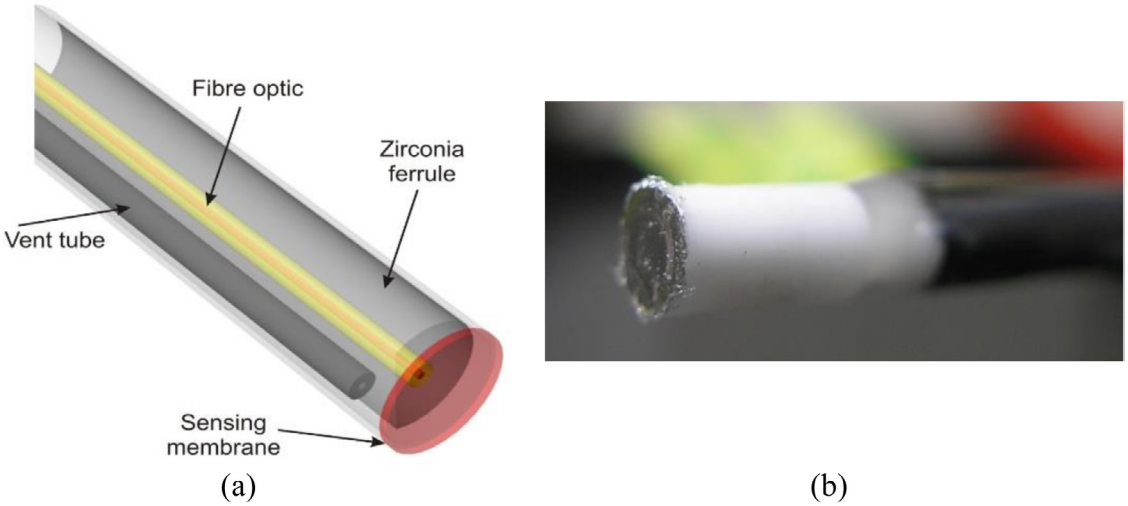

Figure 2. (a) Schematic and (b) photograph of the EFFPI pressure sensor.

a thickness of 0.9 mm, attached using cyanoacrylate adhesive. The sample plate was of the same material used on the aircraft structural skin. To verify the performance of the calibration, a 2 mm gauge length resistive foil strain gauge (RFSG) (model 632-124 from RS components) was also mounted on the plate next to the FBG. The optical fibre containing the FBG was connected to a port of a 3 dB directional coupler to facilitate the interrogation of the sensor using a tunable laser (Tunics Plus—3642 HECL) and a photodiode detector. The wavelength scan of the laser was also calibrated during the experiment by passing a portion of the laser output through a gas cell and monitoring the transmission using a photodiode. The gas cell contained a mixture of CO and HCN, which produced a number of well-defined absorption features in the transmission spectrum. The outputs from the two photodiodes were recorded on a PC via a data acquisition card (NI-6110), while the RSFG was monitored using a strain gauge signal conditioning module from NI SCC-SG01 on a SC-2345 shield carrier connected to the same PC. The Bragg wavelength was determined by fitting a polynomial to the spectrum and differentiating to determine the location of the peak. The resulting calibration curve is shown in figure 1. Here the FBG repeatability is better than 0.29% of full scale over a range of 600 $\mu\varepsilon$. This compares with 0.41% from the conventional strain gauge system.

2.2. Extrinsic fibre Fabry–Perot (EFFPI) unsteady pressure sensor

The following section outlines the basic design of the EFFPI sensor and then describes the calibration procedure. There is also a discussion of the calibration of the sensor using the SmartScan FBG interrogator that was used for inflight measurements, and of the data processing approach adopted, as there were specific limitations due to the interrogator design.

2.2.1. EFFPI sensor design. The EFFPI based fibre optic pressure sensor consists of an optical cavity formed between the end face of an optical fibre and a flexible diaphragm (sensing membrane). As the static pressure changes at the diaphragm, changes in the separation of the fibre-end and the diaphragm can be measured interferometrically.

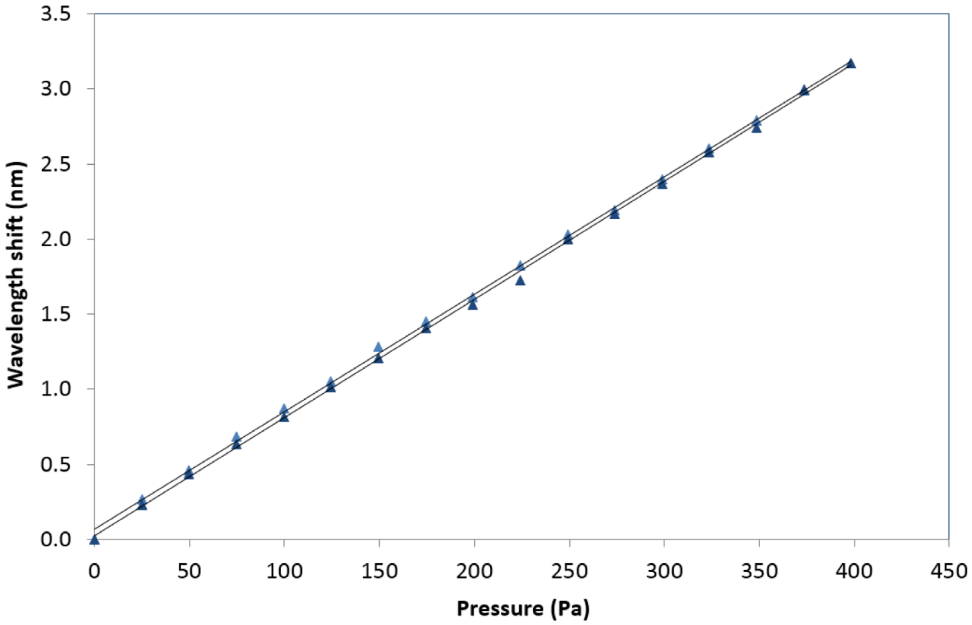

Figure 3. EFFPI calibration curve

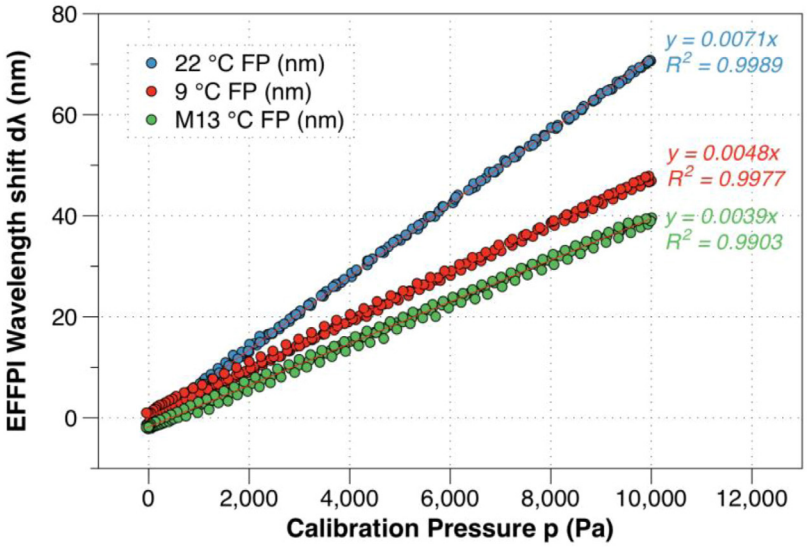

Figure 4. EFFPI Calibration curve variation with temperatures 22 °C, 9.2 °C and −13.5 °C.

A schematic diagram of the EFFPI is shown in figure 2(a). The optical fibre was glued into 10.52 mm long cylindrical ceramic ferrule with an outer diameter of 2.43 mm, typical of those found within an FC/PC fibre optic connector, and its end-face was polished. The side of the ferrule, parallel to the longitudinal axis, was also polished such that the ferrule had a 'D' shape. The ferrule was inserted into a zirconia sleeve (2.5/3.5 mm internal/external diameter and 6.3 mm long) from Senko, and a tube of outer diameter 560 μm and inner diameter 381 μm was also inserted, to act as a vent, such that a differential pressure sensor could be formed. The diaphragm used was a thin electret metallised Mylar film microphone membrane chosen due to its suitable frequency responses (up to 20 kHz) that matched the requirements of the application and the characteristics of the interrogation system. The diaphragm was attached to the zirconia sleeve using Cyanoacrylate and Epoxy resin adhesives.

The optical fibre was connected to the 2nd port of a 3-port circulator, and the reflection spectrum recorded by connecting the tuneable laser (Tunics plus, wavelength scan range 1525 nm–1625 nm) to the 1st port, and a photodiode to the 3rd port. The position of the ferrule within the sleeve was varied, and as the fibre end approached the diaphragm the channelled reflection spectrum characteristic of an EFFPI was monitored. The fibre was positioned such that 10 periods of the channelled spectrum were observed over a wavelength range of 27.45 nm, corresponding to a cavity length of 387 μm. This fringe separation was chosen to provide broad fringes necessary for the low wavelength resolution interrogator used for the flight measurements and to increase the amount of light reflected by the membrane. The ferrule was then glued in position and the system sealed using epoxy resin, as illustrated in figure 2.

The laboratory calibration of the Fabry–Perot sensor and wind tunnel measurements were completed using a wavelength

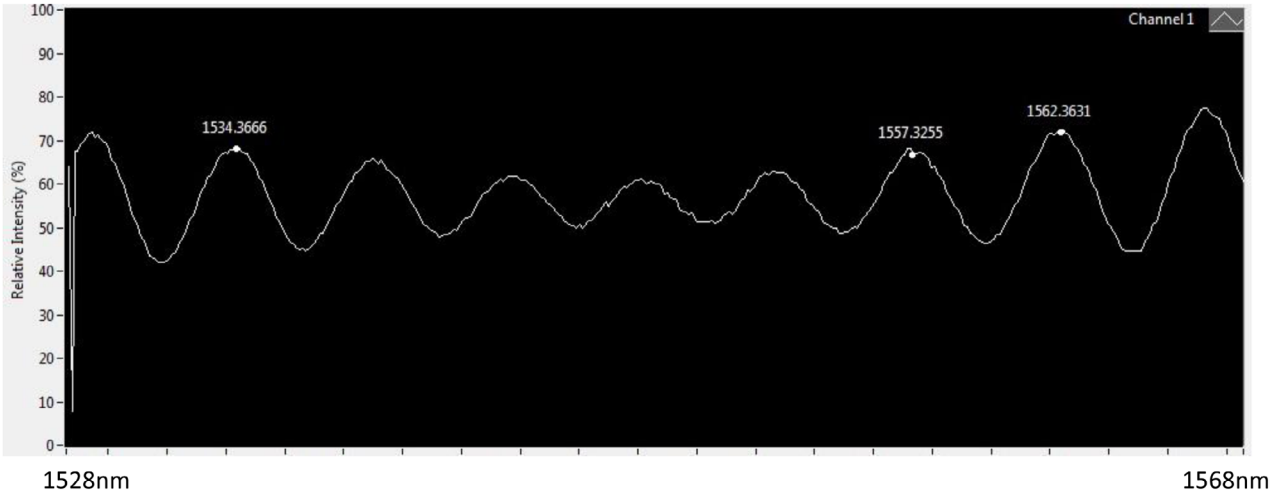

Figure 5. EFFPI spectrum as viewed in the Smartscan monitoring window with 3 tracked signal peaks.

tuneable laser source (Santec HSL 2000), 2 optical detectors (New Focus 2011-FC), an optical coupler network and a high speed (2 GS s^{-1}) data acquisition system (NI PXI 5152 card on a NI PXI 1033 chassis) controlled by a PC. The output from the laser was tuned through the optical spectrum (1262.5–1311.5 nm) at a frequency of 2.5 kHz. The 3 dB bandwidth was 1.6 nm

The resulting calibration curve is shown in figure 3. Here, the resolution of the system is better than 0.33% of full scale over a range of 400 Pa. A conventional Kulite pressure sensor model XCQ-093 (2 psi range) was also mounted adjacent to the Fabry–Perot sensor to validate the EFFPI measurements during the flight test and wind tunnel measurements. The sensor was calibrated using a Druck DPI610 over the expected wind tunnel and flight test working range. The Kulite calibration showed acceptable linearity and a resolution better than 0.15% over a working range of 250 Pa.

2.2.2. EFFPI flight test calibration and data processing. Working in the laboratory and wind tunnel allowed the performance of the EFFPI sensor to be evaluated in a constant temperature environment. The tuneable laser source and acquisition systems used for the initial EFFPI calibration were used to characterise the performance of the sensor in the wind tunnel. The flight test system to be flown on the Bulldog aircraft, however, required an acquisition system certified with respect to airworthiness Certification Specification 23 (CS-23). This requirement resulted in selection of the SmartScan Aero Interrogator box and a further requirement for bespoke post-posting Labview software, which will be outlined later in this section. The SmartScan Aero box meets the requirements for CS-23.

The other difference encountered when using the EFFPI sensor in a flight test situation is the variation of temperature during the flight, which varies with the ambient conditions, including changes in altitude. Hence, a further calibration of the EFFPI sensor was completed in the laboratory, at three different temperatures and also using the SmartScan Aero interrogator to acquire the data. The sensor was calibrated at 22 °C, 9.2 °C and −13.5 °C, and in each case the sensor was allowed to stabilise for up to an hour before data was recorded. The sensor was then connected to a Druck DPI610 and calibrated over a range up to 10 000 Pa, with a repeat of the increase and decrease in pressure in each case. The central wavelengths of peaks in the channelled spectrum reflected from the EFPPI, determined by the Smartscan Aero interrogator, were then processed using bespoke software written in Labview to generate the calibration curves presented in figure 4. Here the calibration functions were $d\lambda = 0.00708p$ (22 °C), $d\lambda = 0.00479p$ (9.2 °C) and $d\lambda = 0.00386p$ (−13.5 °C), where 95% confidence intervals were ±2.15% ((22 °C), ±4.17% (9.2 °C) and ±4.92% (−13.5 °C).

The calibration curve temperature dependency was then converted using Matlab into a two-exponent function of the form:

$$C_{FP} = 0.4458\, e^{-0.01933\, T} + 6.35 \times 10^{-9}\, e^{0.04642\, T} \qquad (1)$$

where C_{FP} is the calibration coefficient and T is the temperature of the sensor in degrees Kelvin.

An example EFFPI spectrum output in the Smartscan monitoring window is shown in figure 5. The spectral peaks which are being measured are also visible. To interpret the data output from Smartscan Aero interrogator, which was in the form of a time series of spectral peak wavelengths, Labview code was developed to post-process the recorded wavelengths of the channelled spectrum peaks. The EFFPI channelled spectrum is windowed by the wavelength range of the scanning laser in the SmartScan interrogator. For the cavity length used here, 8 periods of the channelled spectrum lay within this range.

The peak finding algorithm used in the interrogator stores the peak wavelengths in order, from low to high wavelengths, building a 2D array with each column representing a peak found in the spectrum, and each row recording the wavelengths of the peaks at a particular time. A pressure change induces a change in the phase of the channelled spectrum, and thus a change in the recorded peak wavelengths. An issue arises when the pressure change is such that a peak at one extreme of the wavelength range moves out of range and a new peak enters at the other extreme. This results in a step in the wavelengths recorded in a column of the array,

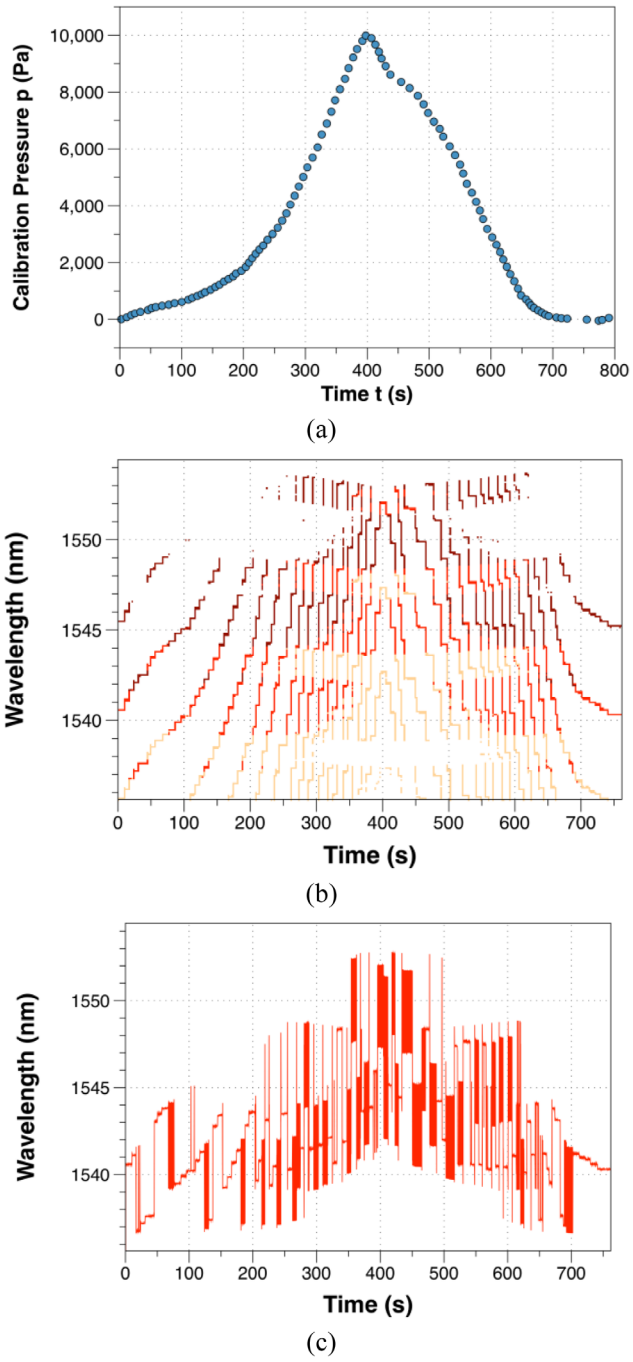

Figure 6. (a) Pressure applied to the EFFPI sensor (b) complete raw data (c) typical raw data sample.

as effectively the numbering of each peak in the channelled spectrum is increased or decreased by 1. This 'peak-skipping' is a common feature of fringe based optical sensors, which generates a π-phase ambiguity problem which requires fringe processing algorithms to reconstruct absolute measurement values, in this case the EFFPI diaphragm position [27–30]. Figure 5 shows experimental data recorded as the pressure experienced by the EFFPI was varied using the Druck DPI610 pressure calibrator. Figure 6(a) shows the applied pressure. In this case, 3 peaks of the EFFPI channelled spectrum were tracked by the Smartscan Interrogator. Figure 6(b) shows the time series of the recorded central wavelengths, where lines show the data recorded in columns 1, 2 and 3 of the data array. Figure 6(c) shows recorded peak wavelength of the first spectral peak within the window. The peak-skipping effect is apparent. There is also evidence of data dropout as the ability to identify a peak can be compromised the presence of noise in the spectrum. The peak finding algorithm used in the interrogator is optimised to identify Gaussian features in the spectrum, which can limit its ability to identify the peaks of the sinusoidal features of the channelled spectrum.

Figure 7(a) illustrates the action of the algorithm used to overcome these issues. A spectral range—the grey shaded are, is selected, which contains at least 3 spectral peak wavelengths. A peak located near the centre of this range is selected and tracked as the pressure changes. When the peak wavelength reaches an extreme edge of the selected wavelength range, the algorithm selects a new peak wavelength near the centre of the spectral range to track, causing a 'skip' in the trace this is illustrated by the black line. The value of the wavelength skip is added to the newly selected peak wavelength, such that the a wavelength trace appears contiguous, as shown in figure 7(b).

Sources of error associated with EFFPI sensors have been discussed in detail by Qi *et al* [29]. These include errors resulting from the wavelength stability of the laser, peak tracking errors and temperature dependence of the sensor. The wavelength stability of the SmartScan Aero interrogator is quoted as ± 5 pm over a 40 nm range (1528 nm–1568 nm) or 0.0125% of full scale. The wavelength repeatability is stated as better than 1 pm (0.0025%). Hence for the purposes of the following application, these errors are considered negligible. Therefore the remaining temperature and peak tracking errors can be accounted for in the calibration process outlined previously.

It should also be noted, however, that the random error in the calibration data was also dependent on the number of peaks tracked. This dependency is apparent in the calibration data (see figure 4), where it was found the data variance increased with decreasing sensor temperature. This increased noise generated more frequent data dropouts, resulting in a lower peak tracking count that fell from 5 peaks at 22 °C to 3 peaks at −13.5 °C, with RMS spectral error increasing from 0.776 nm to 1.32 nm. The other effect which increased data dropout was the change in the amplitude distribution in the EFFPI channelled spectrum. In this case, it was found that the mid-spectral range features reduced in intensity with decreasing temperature. This effect became more problematic for the SmartScan peak identification algorithm, which relies on fixed overall signal to noise setting for all peaks but with local spectral range intensity amplification. Therefore, as the peak-to-peak amplitude range increased with decreasing temperature, the overall data dropout was found to increase, thus increasing noise.

2.3. Wind tunnel and computational fluid dynamic testing of the Fabry–Perot pressure sensor

Before flight testing the EFFPI pressure sensor, preparatory work was completed using a combination of wind tunnel testing and computational fluid dynamics (CFD). The CFD

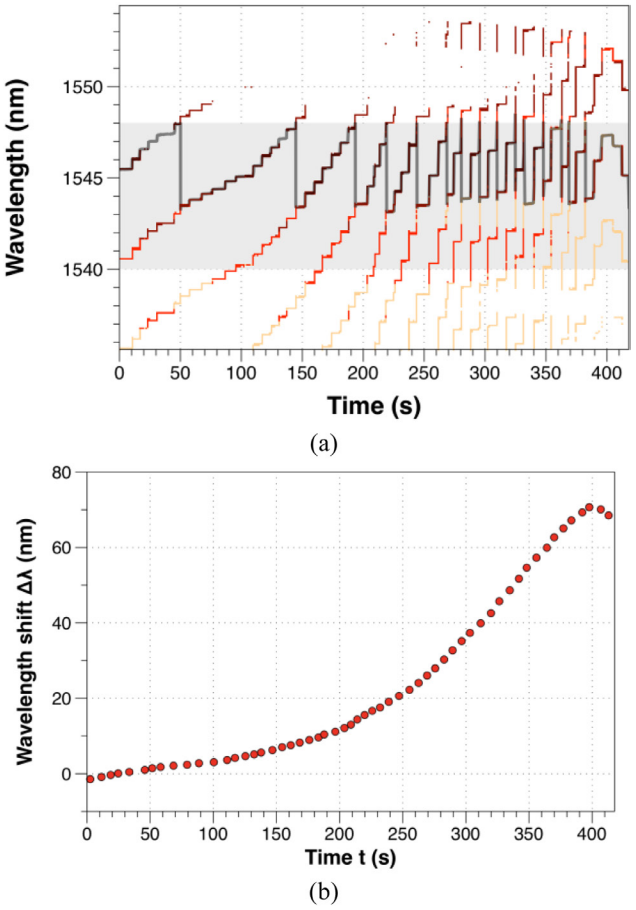

Figure 7. (a) Raw data sample with spectral peak search range (grey) (b) processed spectral peak data.

was used to assess the location of the pressure sensor on the aircraft in terms of expected pressure characteristics. The wind tunnel testing was used to validate the CFD and to test the EFFPI sensor for robustness, including checking its performance alongside a conventional Kulite sensor. The wind tunnel set-up and CFD studies are outlined in more detail in previous work, which used a 30% scale model and a test plate with equivalent scaled sensor positions [31, 32]. The CFD solution showed an expected pressure coefficient increase of around $\Delta C_p = 0.05$ with an increase in angle of attack from 4° to 12°. This ΔC_p is equivalent to a pressure change of around 30–120 Pa at sea level conditions and typical aircraft flight speeds.

Figure 8 shows the data obtained from the EFFPI and Kulite pressure sensors during the wind tunnel testing, over a range of angle of attack from −2° to 15°. The plot also includes C_p data obtained from a conventional static tap located adjacent to the Kulite and EFFPI sensors. Previous error analysis for the static pressure system has shown an error of ±1.44% of full scale [31]. Calibration of the Kulite over a 200 Pa range showed an error ±0.14% of measured scale. The results show that, within experimental error, the EFFPI sensor captures correctly both the C_p values and the ΔC_p increase across the investigated range of angles of attack when compared to the conventional pressure sensor data. This ΔC_p increase is also consistent with the CFD solutions outlined in [31]. There is clear positive offset, however, between the Kulite and the EFFPI and static tap data of around C_p 0.01. This offset is outside the calibrated error range of the sensors. There has also been an additional CFD study of the effect of the beacon structure on the sensors pressure distribution [33]. The beacon structure is positioned downstream of the sensors on the aircraft, but not in the wind tunnel model. This study found a dependency of the pressure field on flow sideslip angle which was of the same of magnitude as the measured range. However, the wind tunnel model was assumed to have negligible sideslip angle and no beacon. Therefore further work is required to understand this discrepancy.

3. Bulldog flight test platform

To flight test the fibre optic strain and pressure sensors, the Bulldog light aircraft was modified under certification standard CS-23 as a minor modification to allow the carriage of a fibre optic interrogation unit and the fibre optic sensors. In order to validate the data from the EFFPI pressure sensor, a conventional Kulite pressure sensor was installed adjacent to the EFFPI and connected to a data logging unit. More specifically, with reference to figure 9, the equipment installed was:

- Power supply box (0.36 kW)
- United Electronic Industries (UEI) data logging cube + trigger box
- SBG Systems SBG Systems IG-500A-G4A2P1-B AHRS
- SmartScan Aero fibre optic interrogation box;
- Optical fibre with 5 FBGs mounted onto the upper wing surface;
- EFFPI sensor mounted onto a fuselage test plate;
- XCQ-093 Kulite pressure sensor mounted onto the fuselage test plate
- On-board cockpit mount and camera

The use of a lightweight replacement mounting plate for the instrumentation boxes, resulted in a net aircraft weight increase of 13 kg without any significant change to the centre of gravity. As the Bulldog aircraft is in the aerobatic category, this certification standard permits tests in the flight envelope −4g to +6g and spinning. The SmartScan Aero interrogator was used to interrogate both the FBG and the EFFPI sensors.

As indicated by figure 9, the FBG strain sensing system consisted of a single fibre containing five wavelength division multiplexed FBGS connected to one channel of a SmartScan Aero FBG interrogator. The SmartScan interrogator is an aerospace certified interrogator capable of scanning a 40 nm wavelength range at 2.5 kHz, with a wavelength repeatability better than 1 pm. It is a standalone unit capable of tracking the FBGs peaks and storing the data to a removable storage drive. The spanwise positions of the FBGs on the wing spar relative to mainplane station 26 are listed in table 1. Four of the five FBGs were mounted onto the surface above the wing spar using cyanoacrylate adhesive. The fibre section with the fifth grating was then fed into a hypodermic tube section and allowed to 'float' inside the tube to measure only temperature and thus

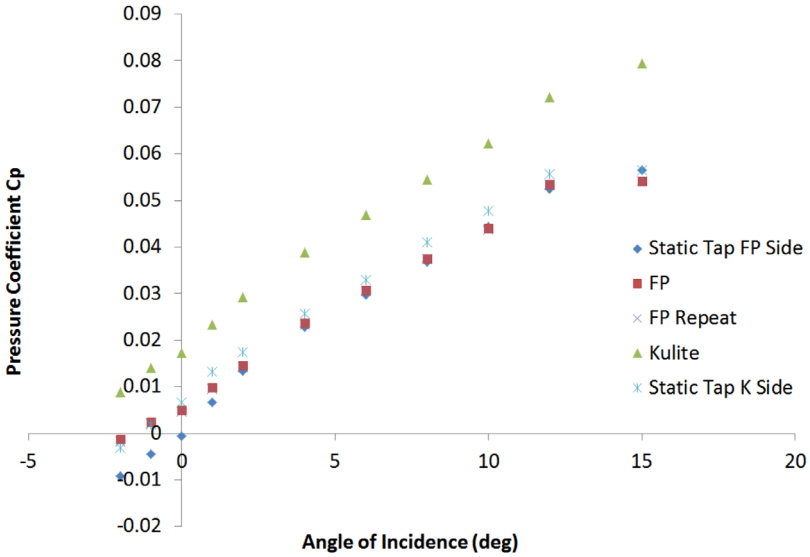

Figure 8. Wind tunnel test plate pressure coefficient characteristics.

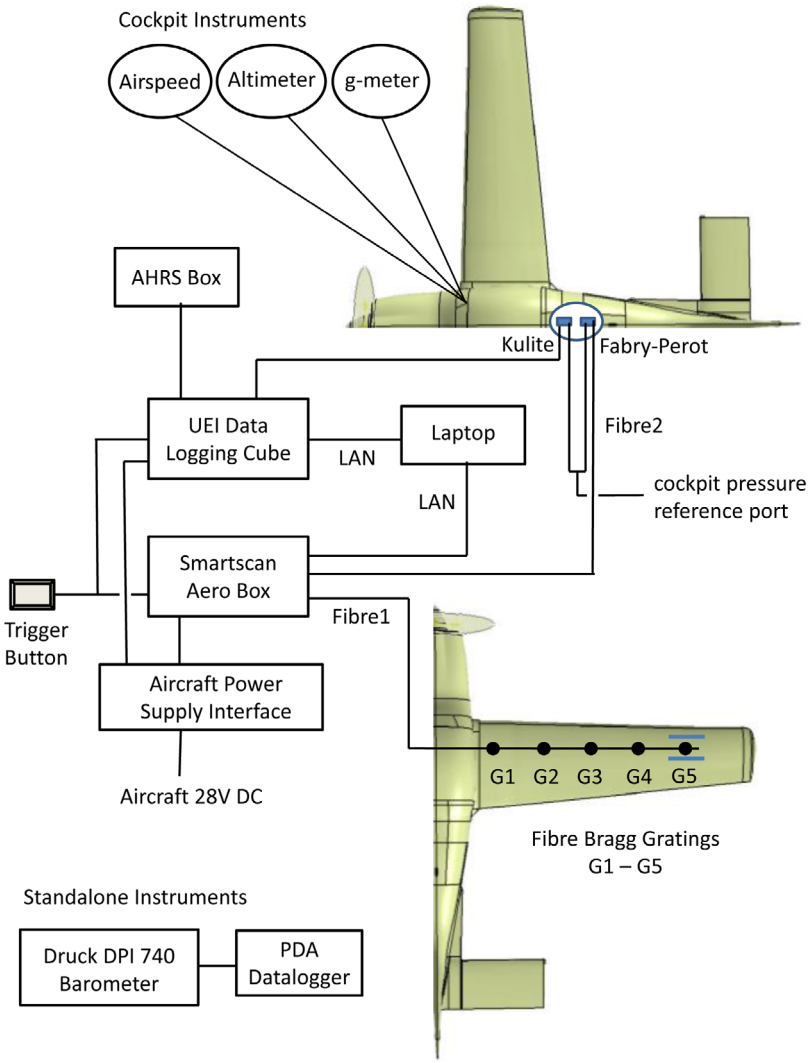

Figure 9. Bulldog instrumentation set-up.

facilitate temperature compensation of the stain measurements made by the other FBGs in the array. The hypodermic sheath was also mounted adjacent to the wing spar at the end of the fibre. Pre-flight, conventional RSFGs (model 632-124 from RS components) were fitted adjacent to the 4 strain—measuring FBGs to check the laboratory FBG calibration. No significant

Table 1. FBG spanwise positions relative to mainplane station 26.

Grating number	Grating spanwise position (mm)
1	200
2	400
3	1200
4	2200
5 (temperature datum)	2600

change to the laboratory calibration was found when the wing tip was deflected and the strain measurements from the FBGs and the RSFG were compared. The RFSG wiring was then removed for the flights and the optical fibre on the wing was covered with a protective length of 3M 425-50 aluminium speed tape.

The EFFPI and Kulite pressure sensors were mounted onto a 162 mm diameter test plate positioned on top of the fuselage behind the cockpit. This plate was chosen to ease certification issues as the same access plate had been previously fitted for another flight test application. The two sensors were fitted either side of the aircraft centreline, as shown in figure 10 and loomed through the cockpit rear bulkhead to the SmartScan Aero interrogator and the UEI data cube. Each sensor had a reference pressure port, which was combined using a T-connector and then fed through a single pitot static tube on the wiring loom back into the cockpit. This arrangement ensured relative pressure measurement from the sensors throughout the flight test.

A number of additional instruments were installed, including an IG-500A attitude and heading reference system (AHRS) and a number of temporary standalone instruments including a Druck DPI 740 barometer connected to a data logging personal digital assistant (PDA) (to measure the pressure in the cockpit) and a CMOS 50 Hz ActionCam mounted in the roof of the cockpit. The camera view also allowed monitoring of a number of primary cockpit instruments during the flight as well as visual references from the external view. The AHRS allowed monitoring of three angular rates and accelerations in the longitudinal, lateral and directional axes and the standalone barometric system allowed logging of the atmospheric pressure to within a resolution of 10 Pa throughout the flights. The barometric data was used to provide an effective reference pressure and monitor altitude to allow the calculation of absolute pressures and pressure coefficients for the test flights. Standard cockpit instruments such as the airspeed indicator, the altimeter and the g-meter were also used to record the steady and unsteady flight conditions.

Synchronisation of all the data sources from the flight test was achieved by use of high energy flight manoeuvre including a loop or spin whereby pertinent features in the data traces were used to align all the different asynchronous data sources. It is estimated that this allowed synchronisation to better than 0.5 s.

4. Bulldog flight test program

In order to test the performance of the fibre optic strain and pressure sensors, a series of seven flight tests were completed in the Bulldog over a wide range of flight conditions. In the first six flight tests, problems were encountered with a number of the instruments and on-board systems including data storage issues, a generator failure, Kulite earthing faults and lifting of the protective wing tape from the FBGs in flight. On the seventh flight all systems were working normally and a set of steady state and dynamic manoeuvres were completed over 37 airborne minutes. The steady state flight conditions (two airspeeds) were used primarily to obtain a number of pressures and pressure coefficients for comparison between sensors and for comparisons with previous wind tunnel measurements [31], whilst the dynamic or aerobatic manoeuvres allowed the sensors to be tested over a wide range of normal g-loads. As the data rates of all the sensors were between 1 kHz–2.5 kHz, the temporal resolution of the sensors was expected to exceed the frequencies of interest during the dynamic manoeuvres.

4.1. Overall flight test results

An outline of the flight test profile is shown in figure 11 and table 2 outlines details of the spin and aerobatic manoeuvres. The ambient temperature profile of the flight was calculated using an adiabatic lapse rate of 1.98 °C per 1000 feet which was based on the use of International Standard Atmosphere (ISA) estimations. This temperature profile closely matched meteorological forecasts for the day with an airfield elevation temperature of 23 °C at the time of the flight. This ambient temperature profile along with equation (1) was used to temperature correct the EFFPI data. Temperature corrections to the FBG were completed using the 5th FBG as outlined in section 3.

Figure 12 illustrates the corresponding barometric and EFFPI pressure profiles for the flight where the barometric profile is represented in terms of a pressure change relative to the take-off or airfield ambient pressure. The time is defined from the take-off point of the flight. The FBG data is also included and the flight profile is clearly visible from the barometric data and a similar profile is also evident from the uncorrected and corrected EFFPI data, where a direct temperature correction has been applied based on the calibration represented in equation (1). The change in pressure in the EFFPI data, however, greatly exceeds that expected for a relative pressure sensor and the sensor pressure profile looks like the behaviour of an absolute pressure sensor such as the barometer. This unexpected behaviour can only be attributed to a partially blocked static port whereby the absolute barometric pressure will not be fully achieved. This absolute behaviour of the EFFPI sensor is further reinforced if the Kulite pressure data is also examined in figure 12. Here it can be seen, the Kulite pressure change ranges between −400 Pa to +1200 Pa and therefore this sensor is behaving as expected as a relative pressure sensor.

4.2. Straight and level flight test results

To compare the general performance of the EFFPI and Kulite pressure sensors, two straight and level conditions were flown at a cruise altitude of 8400 feet on an altimeter standard pressure setting of 1013 millibars. This altitude was selected to

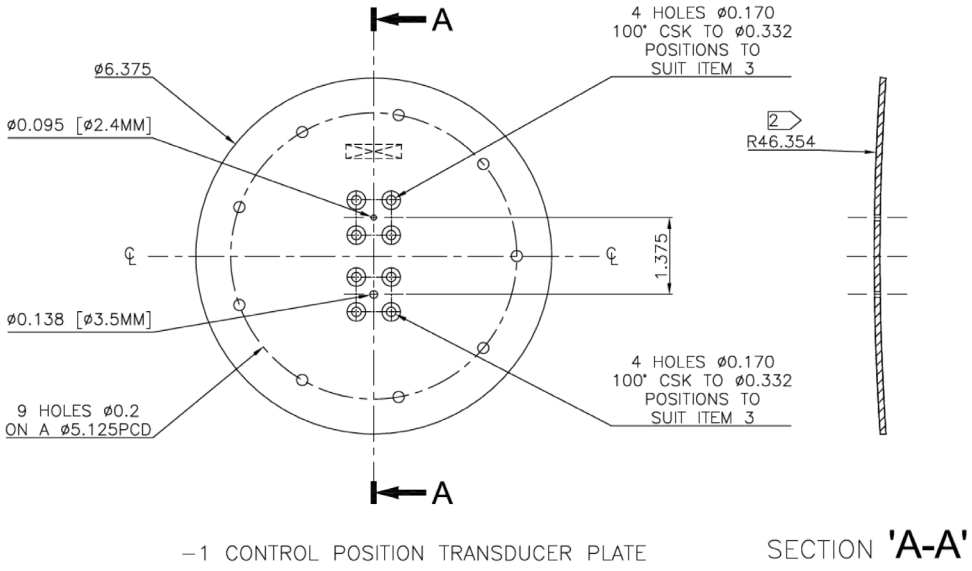

Figure 10. Bulldog pressure sensor mounting plate.

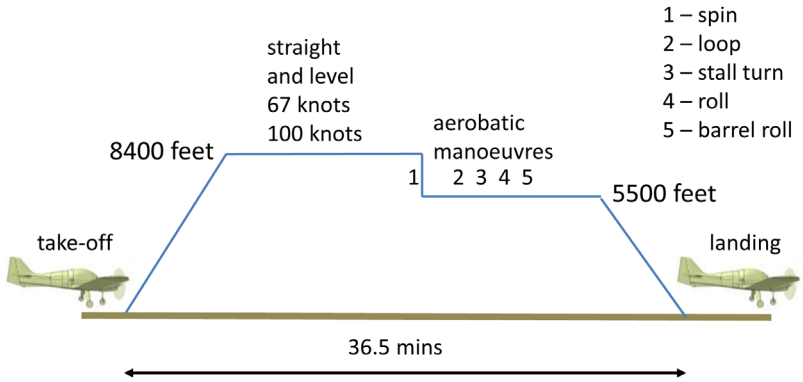

Figure 11. Flight test profile—flight 7.

Table 2. Spin and aerobatic manoeuvre profiles—flight 7.

Manoeuvre	Entry speed (knots)	Minimum g-load	Maximum g-load
Spin	60—stall	1	4—during pullout
Loop	145	0.5	4
Stall turn	120	0	4
Roll	120	−1	1.5
Barrel roll	140	0.5	3

ensure that the test was conducted in smooth air. On the day of the tests in July 2014, the lower air mass was unstable with cumulus cloud formation up to around 7500 feet. Therefore, about 500 feet above the cloud tops, the air mass stabilised and, after manoeuvring and trimming the aircraft and also including a further margin above the cloud tops, a set of stable measurements were made at 8400 feet. To ensure a consistent sample, the Druck 740 barometer was used to monitor the barometric pressure in the cockpit during the measurements with the sample set assumed valid with a variation in barometric pressure of less than ±10 Pa during the sample period. This criterion was based on the stated Druck 740 resolution of 10 Pa and as 1 mbar or 100 Pa of pressure change equates to approximately 30 feet change of altitude. This required the pilot to maintain the altitude of the aircraft to within 1 m (~3 feet) over the sample period.

Figure 13 shows a sample of the straight and level data recorded over 5 s periods for two flight conditions of 67 knots and 100 knots that met the 10 Pa criterion with the rms in pressure of 0.3% for the Kulite raising to around 3% for the Fabry–Perot.

As the sampling frequencies of the Druck barometer, the Kulite and the EFFPI pressure sensor were different, an averaging routine was used to align the Kulite and EFFPI data with the Druck sampling frequency. The results show the EFFPI to have consistently higher levels of pressure change for both the flight conditions tested. In both data sets, the pressure increases with reducing airspeed, corresponding to an increase in the angle of attack. In this case, the Kulite indicated a C_p rise of 0.12 while the EFFPI shows around twice the equivalent pressure raise. The rise in C_p or pressure with reducing airspeed is consistent with computational and wind tunnel results [31] with an angle of attack increase of 4° (100 knots)–9° (67 knots) [32]. Similar trends are found in the wind tunnel results in figure 8. At this stage, however, the difference in the level of C_p for the Kulite and the difference in pressure change between the Kulite and EFFPI sensors exceeds the calibration errors. It is not clear what has caused this

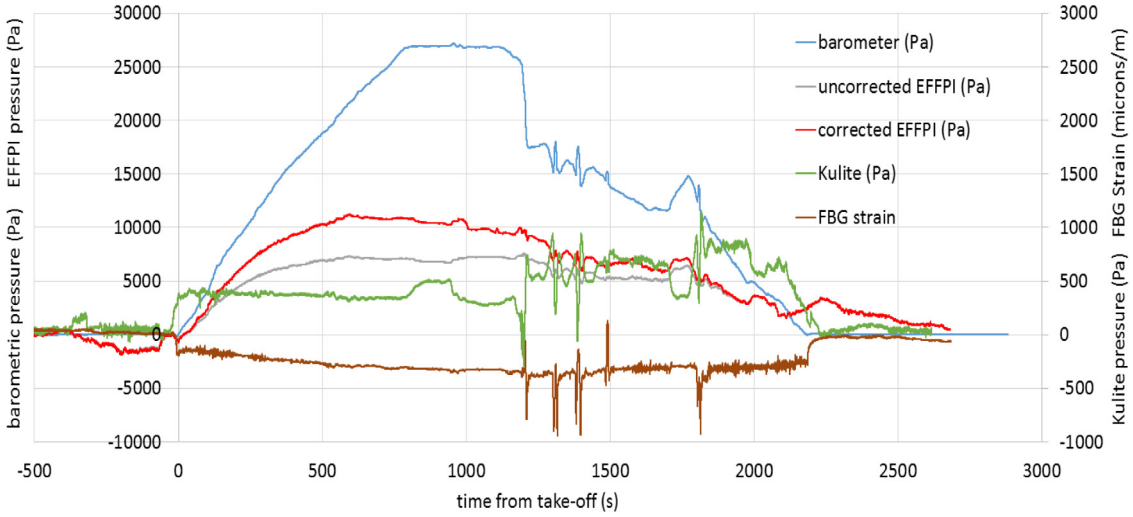

Figure 12. Barometric, EFFPI, Kulite and FBG flight profile data—flight 7.

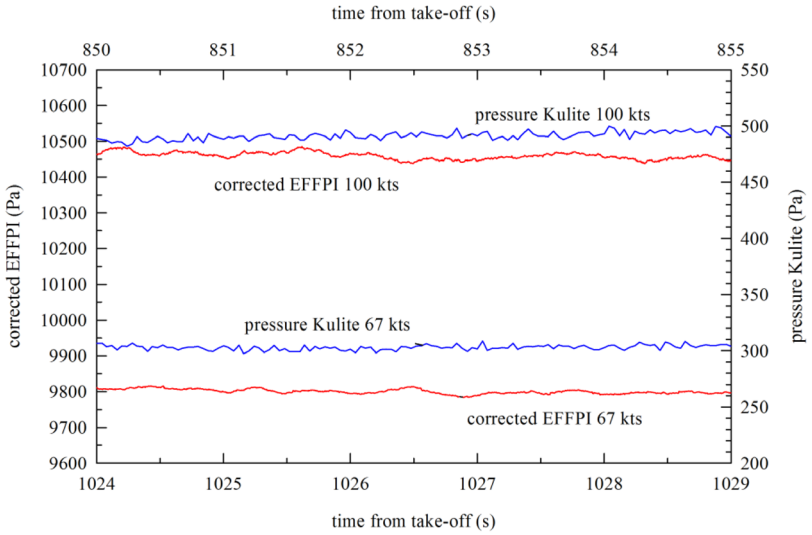

Figure 13. Samples of EFFPI and Kulite pressure data from Bulldog flight test.

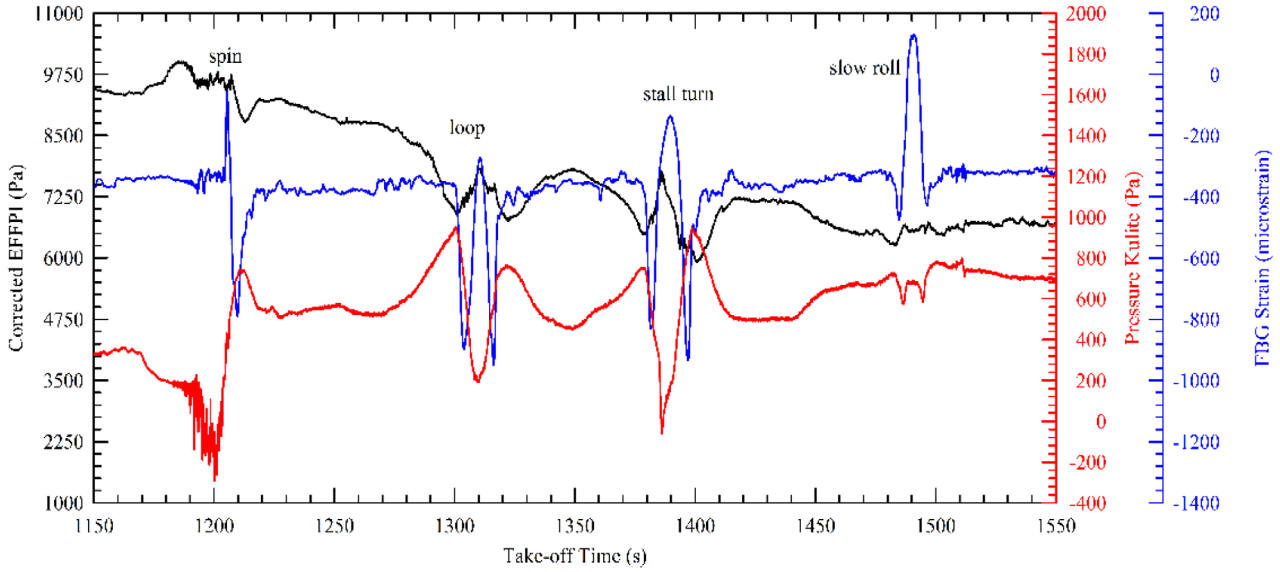

Figure 14. EFFPI, Kulite pressure data and FBG strain data from dynamic Bulldog manoeuvres.

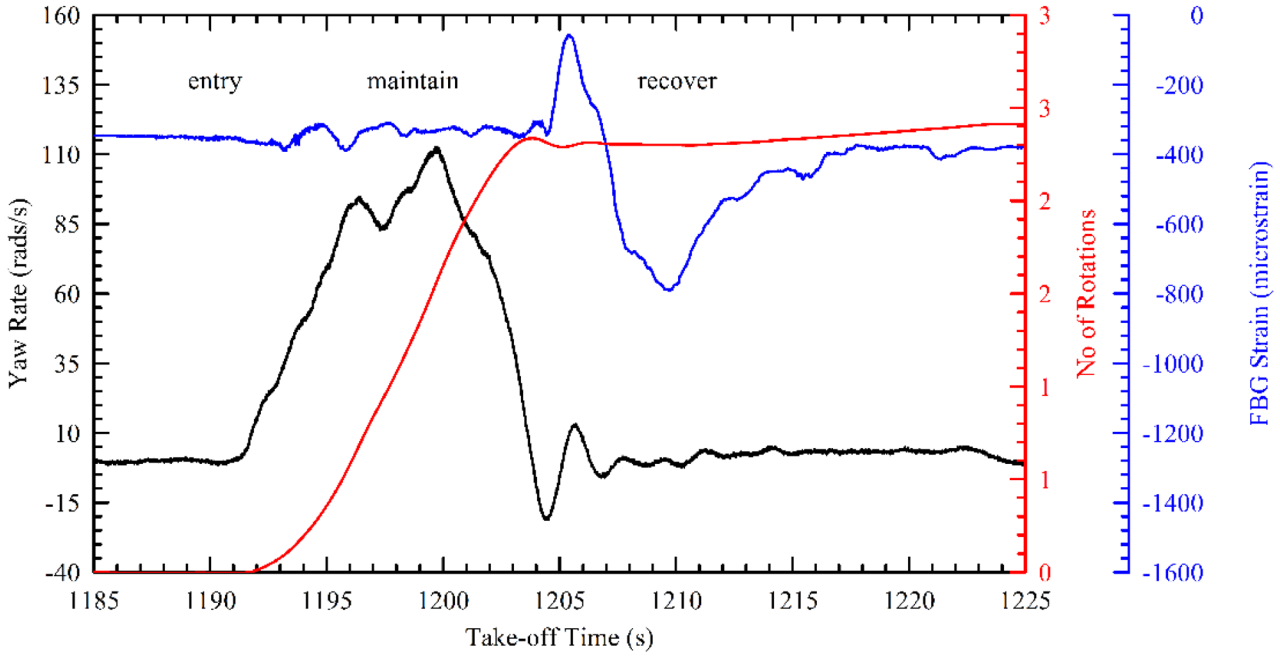

Figure 15. AHRS and FBG strain data for the spin manoeuvre including integration of the spin rotations.

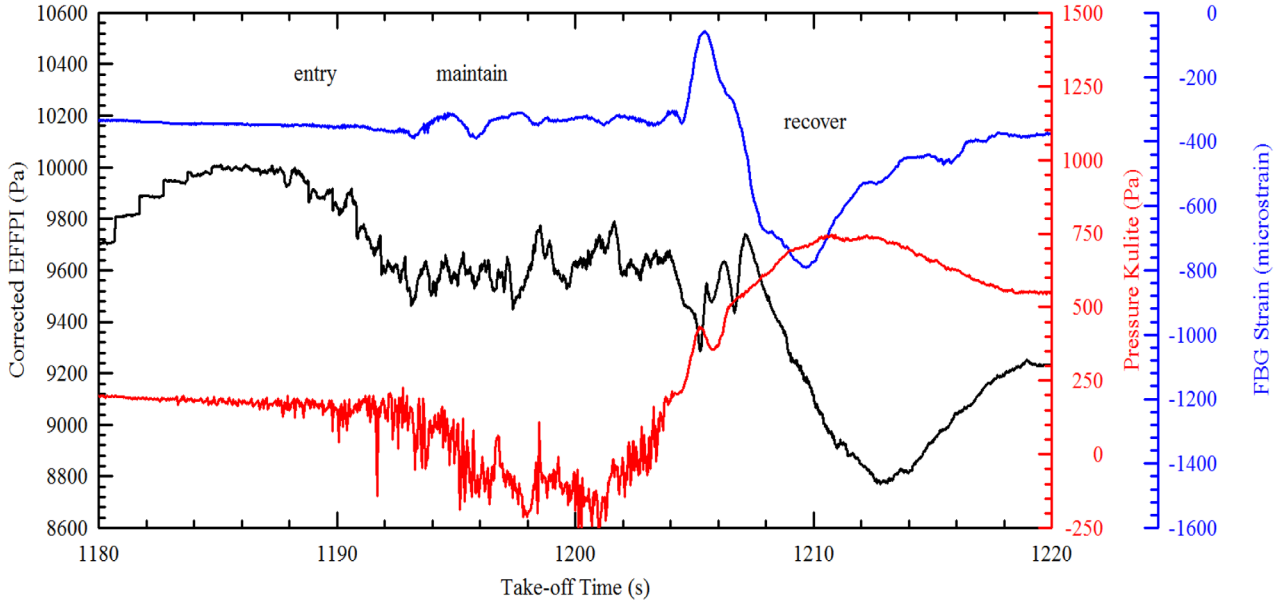

Figure 16. FBG strain data and EFFPI and Kulite pressure data for the spin manoeuvre.

discrepancy. Further computational work has investigated a number of parameters including the effect of protuberances adjacent to the pressure sensor test plate such as the aerial and high intensity beacon [33]. This CFD work did account for minor changes in local pressure and C_p, but not at a sufficient level to account for the changes found in this test. The calibration result in figure 4 shows a significant temperature dependence of the EFFPI sensor, which could account for part of these differences as the sensor may not have stabilised in temperature at this point in the flight and therefore the EFFPI correction would not correctly account for the actual temperature of the sensor. This discrepancy is plausible as the complete sensor is not exposed to the ambient conditions, only the diaphragm section of the EFFPI sensor. Hence although the pressure mounting plate may have reached ambient temperature, the complete sensor is likely not to be at this condition.

4.3. Dynamic manoeuvres

Following the straight and level tests, a series of dynamic high-g manoeuvres were performed to check the sensors over a greater performance envelope including strain and pressure changes. Figure 14 illustrates a detailed plot of the strain and pressure dynamic data for four of the five manoeuvres performed where the significant changes are evident at each manoeuvre.

The first dynamic manoeuvre in the flight profile was a spin to the left. After entry, the spin tends to a stable, cyclic flight

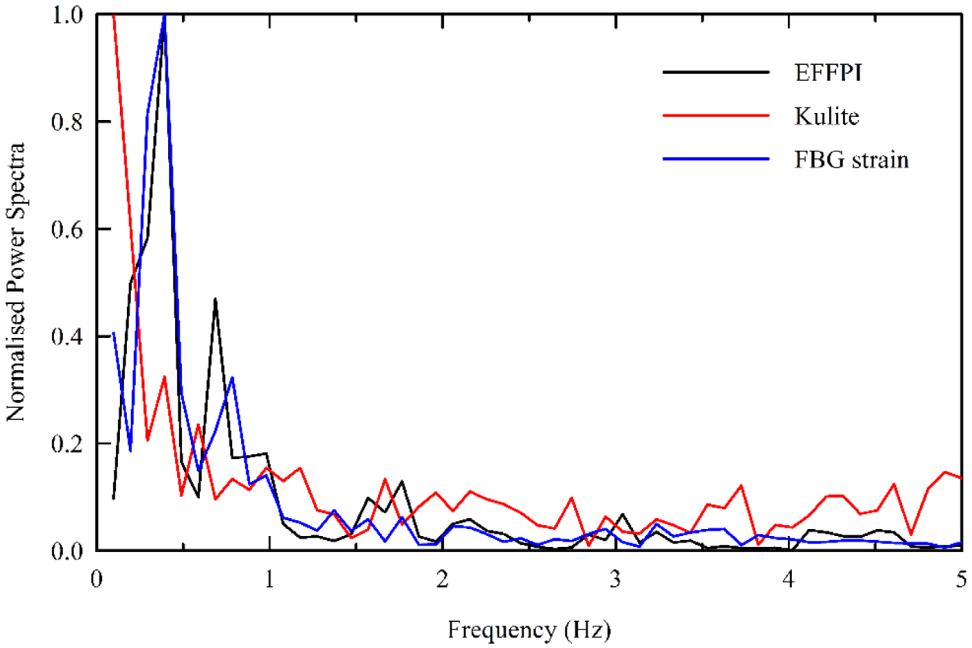

Figure 17. Normalised sensor power spectra from the spin.

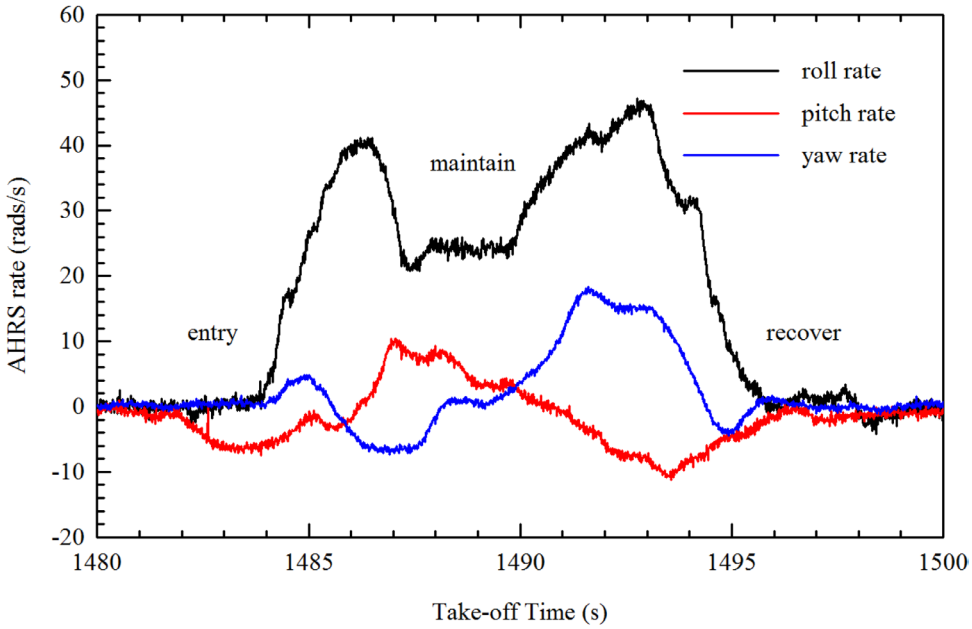

Figure 18. AHRS data during a roll.

1g condition with a near vertical flight path and a high descent rate in excess of 8000 feet min^{-1}. The manoeuvre in this case was initiated at 8400 feet from an aerodynamic stall and maintained for around two aircraft rotations before starting a recovery sequence to straight and level flight which occurred over half a rotation. The time history of the spin in terms of rotations and AHRS yaw rate is shown in figure 15, where the recovery point can be seen in the yaw rate plot which reverses from a positive rate to a negative rate at around 1205 s in the flight profile.

The data recorded from the fibre optic sensors during this spin sequence is illustrated in figure 16 where the Kulite data is included for comparison. If the EFFPI pressure data is examined, the spin rotations are evident in the data as cyclic changes in amplitude, with the increase in pressure during the recovery in both the Kulite and EFFPI data. The Kulite data, however, appears to have less clear evidence of the spin rotations. This discrepancy is thought to be related to the position of the sensor relative to an aerial that was located adjacent to the sensor plate. The wake characteristics formed downstream of the aerial due to the flight path of the aircraft during the spin would be expected to influence the pressure measured by the Kulite. Previous CFD analysis [33] has reinforced this inference. Further analysis of the data is presented in the power spectra in figure 17, where in this case the spin frequency of 0.4 Hz can be clearly seen in the EFFPI and FBG strain data,

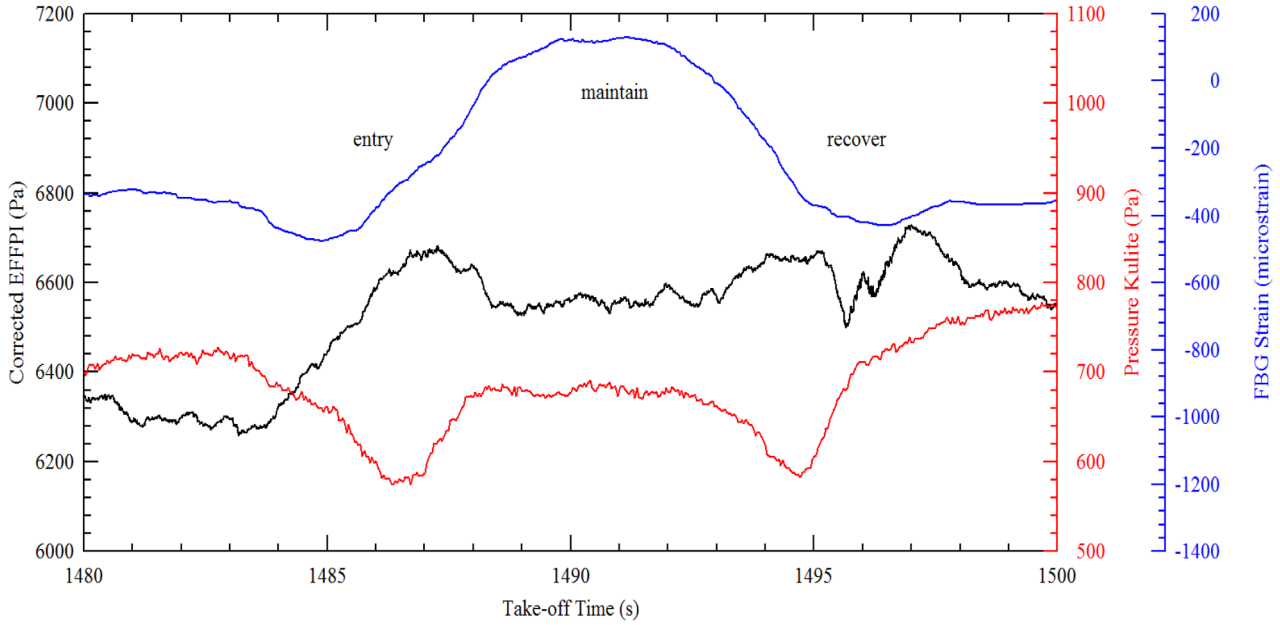

Figure 19. FBG strain data and EFFPI and Kulite pressure data from a roll.

but is not clear in the Kulite data. The frequency of 0.4 Hz was confirmed in a movie recorded using the ActionCam CMOS camera by reference to a repeated ground feature during each rotation. This analysis also gave a period of rotation of 2.6 s, corresponding to 0.4 Hz.

Following the spin, a further four dynamic manoeuvres were completed, including a loop, a stall turn, a roll and a barrel roll over a normal g-range of −1g to +4g. In this case, the g-range limits of the Bulldog are −4g to +6g. Figures 18 and 19 show the data recorded during a roll to the left. In this case, the roll required an initial positive g-load pitch-up during the entry followed by initiation and maintenance of negative 1g during the inverted phase with the final phase, a continuation of the roll to erect straight and level positive 1g flight. These three distinct phases are clearly seen in figures 18 and 19 for the AHRS data and the EFFPI, Kulite and FBG strain data.

Overall, with these manoeuves a normal g-range between −1g to 4g was flown with no issues for the optical fibre based systems and the temporal resolution of the sensors allowed detailed analysis of the dynamic flight profile. To the authors' knowledge, this is the first reported analysis of such aerobatic manouevres using this combination of optical fibre based strain and pressure sensors.

4.4. Dynamic manoeuvres—further analysis

Additional analysis of the dynamic manoeuvres was possible by further processing of the AHRS data with direct comparisons to the wing strain measured by the FBG sensors. For this analysis, the assumption is made that the g-load increment $(n-1)$ of the aircraft during an erect or inverted pull-up manoeuvre is found from:

$$(n-1) = \frac{qV}{g} \tag{2}$$

where V is the aircraft entry speed into the pull-up and q is the pitch rate (rad s^{-1}) obtained from the pull-up [34]. Furthermore, if it is assumed that the aircraft wing semi-span behaves as a simple cantilevered loaded beam with a distributed load W, the maximum surface stress σ at a given position x on the wing span is found from:

$$\sigma = \frac{W(L-x)^2}{2Z} \tag{3}$$

where L is the beam length and Z is the section modulus of the wing [35]. Therefore, at a fixed point x on the wing span, the surface stress is expected to be proportional to the loading or g-load on the wing.

Hence the pitch rate increments for the loop, stall turn, roll and barrel roll were analysed and processed into g-increments $(n-1)$. These were then compared to the corresponding strain recorded by the FBG during the flight. These results are plotted in figure 20, where it can be seen that a strong correlation exists between the g-load on the wing and the local surface strain measured by the FBGs. This confirms that the wing semi-span is behaving similarly to a cantilevered beam system and this type of application of the FBG system is the basis of a simple wing-loading monitoring instrument. To check these results, the AHRS z-axes g-load data was also examined at the same manoeuvre points in the flight. In the majority of cases, the pitch rate g-loads matched to within 15% of the AHRS data, which was an indication of the uncertainty in the pull-up $(n-1)$ load estimates. Based on the FBG calibration, the strain increment had uncertainties of 0.58% of full scale.

5. Discussion

Following the flight tests and given the data presented, there are a number of points for discussion. Firstly, considering the FBG strain measurement system, the simple method of

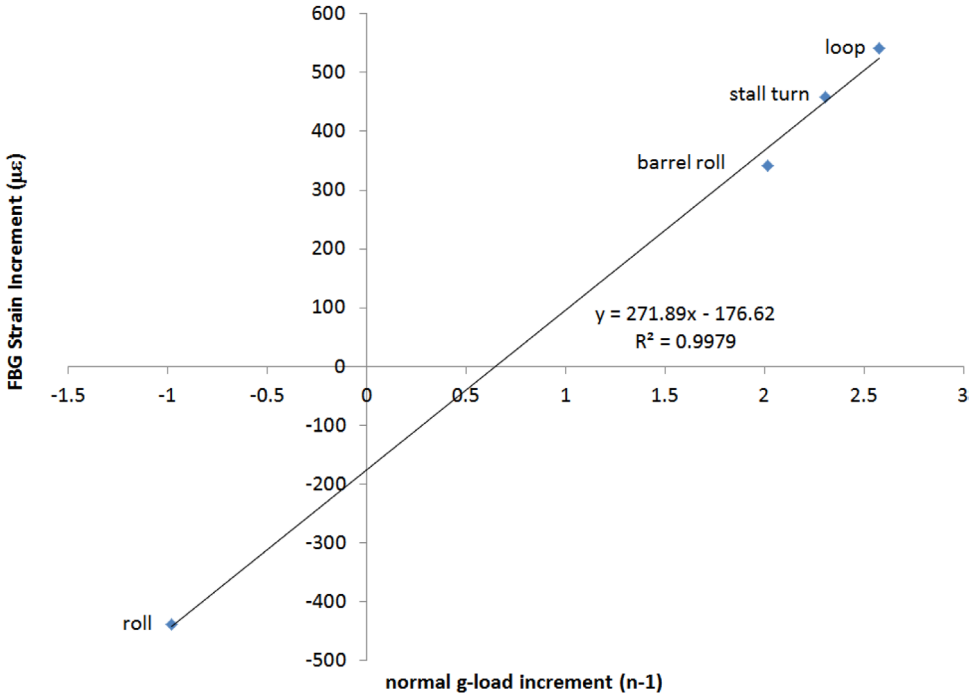

Figure 20. FBG strain data and wing load characteristics from the Bulldog flight test (uncertainty estimates $(n-1)$ $\pm 15\%$, strain increment $\pm 0.58\%$).

attachment of the fibre to the wing surface with cyanoacrylate proved effective and robust. Subsequent use of the aircraft for other flying activities over the previous 18 months and by using 3M 425-50 tape to protect the fibre and FGBs, have resulted in no noticeable degradation of the sensors. Therefore this method of installation of fibre based strain sensors to aircraft surfaces offers a practical flight test monitoring tool, which can be easily removed from the aircraft once the flight test program is complete. Furthermore, given that the speed tape is certified to 250 knots (120 m s^{-1}), this mounting method for the FBGs is also applicable to a wide range of jet and propeller aircraft without any aerodynamic disadvantages. In addition, the 140–250 μm diameter of the fibre ensures a minimum footprint on the surface without any EMC considerations.

In the case of the EFFPI pressure sensor, the integration of the sensor onto the aircraft was relatively straightforward due to the small diameter of the fibre, as it could be fed through space limited areas of the fuselage back into the cockpit and if necessary attached to existing wiring looms without any EMC degradation. In the laboratory and wind tunnel environment, as the complete spectral output of the sensor could be processed, calibrated full scale resolution and bandwidth of the EFFPI sensor was 0.15% at up to 10 kHz, which compares well with equivalent Kulite sensors. The main disadvantage of the EFFPI sensor for flight test, however, was the limitation of the SmartScan peak finding algorithms which were optimised for FBG Gaussian peak characteristics. These could not be changed by the user. Therefore this limitation resulted in non-optimal fringe peak tracking characteristics, leading to data dropout and an order of magnitude less accuracy in the pressure data (rms errors of $\pm 2.15\%$ to $\pm 4.92\%$). These limitations were also combined with the 'fringe skipping' effect in the data due to the significant movement of the sensor diaphragm. Hence bespoke Labview software was required to post-process and reconstruct the data across the full sensor test range. The data dropout effect was further accentuated by changes with temperature to the spectral amplitude distribution of the EFFPI fringes. Typically three EFFPI fringe peaks were tracked reliably during a flight test, whereby a maximum of eight peaks could be tracked per channel with lower fringe noise. Thus, although tracking more peaks would reduce the error to some degree, with 8 peaks reducing the current random error by 40%, ultimately the peaking algorithm needs modification to fit a sinusoidal profile. Such a modification would also offer potential accuracy as high as the wind tunnel and laboratory calculations.

A further consideration of the EFFPI sensor was the dependence of the sensitivity on temperature. The calibration of the sensor across the temperature range $+22\,^{\circ}$C to $-13.5\,^{\circ}$C appeared to offer a simple method to compensate the sensor for temperature variation in flight. Despite what appears to be a partially blocked static port on the sensor, this temperature compensation method was not sufficient. Thus it is likely that the packaging of the sensor onto the aircraft test plate, resulted in a significant temperature gradient between the sensor diaphragm on the fuselage surface and the reminder of the sensor, located inside the fuselage. This temperature variation needs to be compensated for and would require either some form of reference signal from another sensor, additional measurement of the sensor temperature environment or further data processing methods. In the former case, the use of a reference sensor is analogous to the FBG compensation system and in the latter case previous authors [29] have reported methods to compensate for temperature using both the peak and valley characteristics of the EFFPI spectral fringes. The

latter approach would require storage of the complete spectral characteristics during flight.

One final point to note for the EFFPI sensor is the requirement for one processing channel per EFFPI sensor. This latter point compares with the option to interrogate multi-points on a single fibre and single channel using the FBG system. Hence the requirement to find alternative methods to record and process multiple EFFPI sensors simultaneously is an area requiring future work. If these issues can be addressed, the EFFPI sensor offers a significant opportunity to replace traditional pitot and Kulite type sensors for wind tunnel testing and flight test with the EMC, sensitivity and packaging advantages of FBG's.

6. Conclusions

FBG strain sensors and EFFPI pressure sensors have been developed for flight test by using a combination of laboratory tests, wind tunnel tests and flight test in a modified Bulldog aerobatic light aircraft. The FBG strain sensors were used to measure wing surface strain at 5 selected points on the port wing. The EFFPI pressure sensor was wind tunnel tested on a 30% scale model and subsequently flight tested on a test plate mounted behind the fuselage canopy with a conventional Kulite pressure sensor mounted adjacent in order to validate the measurements.

The flight test of the strain sensors showed good performance with a pre-flight laboratory calibration indicating a resolution better than 0.29% of full scale over a range of 600 $\mu\varepsilon$. During the flight test, a series of dynamic manoeuvres were performed including a spin over a g-range of -1g to $+4$g and the FBG strain measurements clearly resolved the surface wing strain and spin frequency during these tests. Subsequent use of the aircraft following the flight tests has also shown the mounting method of the FBGs to be robust with no obvious degradation of sensor performance.

To test the EFFPI pressure sensors, both steady straight and level measurements and dynamic measurements were completed in flight and compared to the conventional Kulite measurements. Although the pre-flight laboratory calibrations indicated the Kulite and EFFPI had resolutions of 0.15% and 0.33% of measured scale respectively, the requirement to use a specific SmartScan interrogator box to certify the aircraft restricted the data acquisition to a non-optimal peak tracking methods. This resulted in rms errors an order magnitude higher than the laboratory and wind tunnel measurements. Bespoke Labview software was also required to reconstruct the data. Further discrepancies also occurred in flight as it is suspect that the static port on the EFFPI sensor became partially blocked. Therefore although the measured change in pressure and pressure coefficient was generally consistent for both sensors, further work is required to verify the reasons for this discrepancy. This includes a more complex method to temperature compensate the EFFPI sensor as a simple calibration temperature compensation was not sufficient. The dynamic EFFPI pressure measurements, however, allowed sufficient resolution of the different manoeuvres including the spin and spin frequency. Further work is thus required to improve the fringe data processing and the number of sensors per channel for a future EFFPI application.

Acknowledgments

The authors would like to acknowledge European Framework 7 funding, contract number 266107 'Advanced In-Flight Measurement 2' and EPSRC Grant number EP/H02252X/1. The authors would also like to thank Mr Paul Dancer from the Cranfield University Aerodynamics Group workshop. (Enquiries for access to the data referred to in this article should be directed to researchdata@cranfield.ac.uk).

References

[1] Borek R and Pool A 1994 *Basic Principles of Flight Test Instrumentation Engineering* (*AGARD and RTO Flight Test Instrumentation Series AGARDograph 160 (AG 160)* vol 1*)*(Paris: North Atlantic Treaty Organization (NATO) Science and Technology Organization (STO))

[2] Boden F, Lawson N, Jentik H W and Kompenhams J 2013 *Advanced In-Flight Measurement Techniques* (Berlin: Springer)

[3] van der Linden J C and Mensink H A 1977 *Linear and Angular Measurement of Aircraft Components* (*AGARD and RTO Flight Test Instrumentation Series AGARDograph 160 (AG 160)* vol 8*)*(Paris: North Atlantic Treaty Organization (NATO) Science and Technology Organization (STO))

[4] Wuest W 1980 *Pressure and Flow Measurement* (*AGARD and RTO Flight Test Instrumentation Series AGARDograph 160 (AG 160)* vol 8*)*(Paris: North Atlantic Treaty Organization (NATO) Science and Technology Organization (STO))

[5] Kottcamp E, Wilhelm H and Kohl D 1976 *Strain Gauge Measurements on Aircraft* (*AGARD and RTO Flight Test Instrumentation Series AGARDograph 160 (AG 160)* vol 7*)*(Paris: North Atlantic Treaty Organization (NATO) Science and Technology Organization (STO))

[6] Trenkle F and Reinhardt M 1973 *In-Flight Temperature Measurements* (*AGARD and RTO Flight Test Instrumentation Series AGARDograph 160 (AG 160)* vol 2*)*(Paris: North Atlantic Treaty Organization (NATO) Science and Technology Organization (STO))

[7] Measures R M 2001 *Structural Monitoring with Fiber Optic Technology* (New York: Academic)

[8] Lee J-R, Ryu C-Y, Koo B-Y, Kang S-G, Hong C-S and Kim C-G 2003 In-flight health monitoring of a subscale wing using a fiber Bragg grating sensor system *Smart Mater. Struct.* **12** 147–55

[9] Betz D, Staudigel L and Trutzel M N 2002 Test of a fiber Bragg grating sensor network for commercial aircraft structures *15th Optical Fiber Sensors Conf. Technical Digest (OFS), 2002* pp 55–8

[10] Trutzel M N, Wauer K, Betz D, Staudigel L, Krumpholz O, Muehlmann H-C, Muellert T and Gleine W 2000 Smart sensing of aviation structures with fiber-optic Bragg grating sensors *Proc. SPIE* **3986** 134

[11] Read I J and Foote P D 2001 Sea and flight trials of optical fibre Bragg grating strain sensing systems *Smart Mater. Struct.* **10** 1085–94

[12] Ko W L, Richards W L and Fleischer V T 2009 Applications of Ko displacement theory to the deformed shape predictions of doubly tapered ikhana wing NASA/TP-2009-214652

[13] Jutte C V, Ko W L, Stephens C A, Bakalyar J A, Richards W L and Parker A R 2011 Deformed shape calculation of a full-scale wing using fiber optic strain data from a ground loads test NASA/TP-2011-215975
[14] Rao Y J 2006 Recent progress in fibre-optic extrinsic Fabry–Perot interferometric sensors *Opt. Fiber Technol.* **12** 227–37
[15] Neson S, Yu M, Zhang X and Hsieh A H 2008 Miniature fiber optic pressure sensor with composite polymer-metal diaphragm for intradiscal pressure measurements *J. Biomed. Opt.* **13** 044040
[16] Tosi D, Macchi E G, Braschi G, Cigada A, Gallati M, Rossi S, Poeggel S, Leen G and Lewis E 2014 Fiber-optic combined FPI/FBG sensors for monitoring of radiofrequency thermal ablation of liver tumors: *ex vivo* experiments *Appl. Opt.* **53** 2136–44
[17] Sharifian S A and Buttsworth D R 2006 Evaluation of glued-diaphragm fibre optic pressure sensors in a shock tube *Shock Waves* **16** 189–97
[18] Gander M J, MacPherson W N, Barton J S, Reuben R L, Jones J D C, Stevens R, Chana K S, Anderson S J and Jones T V 2003 Embedded micromachined fiber-optic Fabry–Perot pressure sensors in aerodynamics applications *IEEE Sens. J.* **3** 102–7
[19] Pulliam W J, Russler P M and Fielder R S 2001 High-temperature high-bandwidth fiber optic MEMS pressure-sensor technology for turbine engine component testing *Proc. SPIE* **4578** 229–38
[20] Liu Y, Lacher A, Wang G, Purekar A and Yu M 2007 Wireless fiber optic sensor system for strain and pressure measurements on a rotor blade *Proc. SPIE* **6770** 67700Y
[21] Cipullo A, Gruca G, Heeck K, De Filippis F, Iannuzzi D, Minardo A and Zeni L 2012 Numerical study of a ferrule-top cantilever optical fiber sensor for wind-tunnel applications and comparison with experimental results *Sensors Actuators* A **178** 17–25
[22] Meltz G, Morey W M and Glenn W H 1989 Formation of Bragg gratings in optic fibres by transverse holographic method *Opt. Lett.* **14** 823–5
[23] Rao Y J 1999 Recent progress in applications of in-fibre Bragg grating sensors *Opt. Laser. Eng.* **31** 297–324
[24] Chehura E, James S W, Tatam R P, Lawson N and Garry K P 2009 Pressure measurements on aircraft wing using phase-shifted fibre Bragg grating sensors *20th Int. Conf. on Optical Fibre Sensors (Edinburgh, 5th–9th Oct 2009)*
[25] Van Els T J 2009 First deminsys (high speed FBG interrogator) flight *Proc. SPIE* **7295** 72950B
[26] Kosters E and Van Els T J 2010 Structural health monitoring and impact detection for primary aircraft structures *Proc. SPIE* **7677** 76770C
[27] Jiang Y and Ding W 2011 Recent developments in fiber optical spectral white-light interferometry *Photonic Sensors* **1** 62–71
[28] Kim S-H, Lee J-J and Kwon D-S 2001 Signal processing algorithm for transmission-type Fabry–Perot interferometric optical fiber sensor *Smart Mater. Struct.* **10** 736–42
[29] Qi B *et al* 2003 Novel data processing techniques for dispersive white light interferometer *Opt. Eng.* **42** 3165–71
[30] Han M, Zhang Y, Shen F, Pickrell G R and Wang A 2004 Signal-processing algorithm for white-light optical fiber extrinsic Fabry–Perot interferometric sensors *Opt. Lett.* **29** 1736–8
[31] Lawson N J, Gautrey J E, Salmon N, Garry K P and Pintiau A 2014 Modelling of a Scottish aviation bulldog using reverse engineering, wind tunnel and numerical methods *IMechE G: J. Aerosp.* **228** 2736–42
[32] Lawson N J, Salmon N, Gautrey J E and Bailey R 2013 Comparison of flight test data with a computational fluid dynamics model of a Scottish aviation bulldog aircraft *Aeronaut. J.* **117** 1273–91
[33] Riou S 2015 CFD and flight test investigation of the bulldog aircraft beacon sructure on a pressure sensor plate *MSc Thesis* Cranfield University
[34] Cook M V 2007 *Flight Dynamics Principles* 2nd edn (Oxford: Butterworth-Heinemann)
[35] Gere J M and Goodno B J 2013 *Mechanics of Materials* 8th edn (Stamford: Global Engineering)

https://dspace.org/

Development and application of optical fibre strain and pressure sensors for in-flight measurements

Lawson, Nicholas J.; Correia, Ricardo N.; James, Stephen W.; Partridge, Matthew; Staines, Stephen E. ...

2016-09-16
IOP Publishing
http://dx.doi.org/10.1088/0957-0233/27/10/104001
Lawson NJ, Correia R, James SW, et al., (2016) Development and application of optical fibre strain and pressure sensors for in-flight measurements. Measurement Science and Technology, Volume 27, Issue 10, Article number 104001

Downloaded from a DSpace repository. https://dspace.org/